AUT Journal of Electrical Engineering
10.22060/EEJ.2026.25994.6031

A Hybrid Series-Parallel Pemanent-Magnet Coaxial Magnetic Gear with Reduced Rare-Earth Usage and Improved Torque Performance

Mojtaba Malakooti Khaledi, Seyed Ahmadreza Afsari Kashani*
Faculty of Electrical and Computer Engineering
University of Kashan
Kashan, Iran
afsari@kashanu.ac.ir

Abstract

This paper proposes a hybrid permanent-magnet coaxial magnetic gear with reduced rare-earth permanent-magnet utilization and improved torque quality. The proposed radial-flux topology employs an asymmetric inner rotor incorporating NdFeB and ferrite permanent-magnets in a series–parallel magnetic circuit, combining Spoke- and V-type magnet arrangements to improve magnetic-flux utilization. An advanced configuration with strategically positioned flux barriers is further developed to mitigate leakage flux and cogging torque. A multi-objective genetic algorithm coupled with finite-element analysis in ANSYS Maxwell 2021-R1 is employed to optimize torque capability, cogging torque, and permanent-magnet-material volume. The optimized configurations are evaluated using 2-D and 3-D finite-element analysis, including electromagnetic performance, flux-density harmonics, and loss characteristics, with 3-D analysis accounting for axial leakage flux and end effects. Compared with the benchmark configuration, the advanced coaxial magnetic gear reduces the cost-equivalent permanent-magnet volume by 15.7% and the high-speed rotor cogging-torque index by 73.7% in 2-D FEM and 73.3% in 3-D FEM, while maintaining comparable average torque and active volume. The 3-D torque per cost-equivalent permanent-magnet volume increases from 153.23 to 185.96 kNm/m³, corresponding to a 21.36% improvement. The advanced topology also reduces high-order harmonic components and hysteresis and eddy-current losses. Transient structural finite-element analysis predicts a maximum rotational speed of approximately 10500 rpm based on a 350-MPa yield-strength criterion. Experimental measurements yield a maximum static torque of 7.61 Nm, compared with 8.48 Nm from 3-D finite-element analysis, corresponding to a 10.2% discrepancy. These results demonstrate improved permanent-magnet-material utilization and torque quality while maintaining comparable torque performance.

Keywords

Magnetic gear, ferrite, rare-earth magnet, finite-element analysis, hybrid permanent-magnet, genetic optimization algorithm.

1. Introduction

Mechanical gears have long been the dominant technology for power transmission in industrial systems. Their fundamental role in kinematic systems has driven continuous advancements aimed at improving manufacturing precision, operational efficiency, torque density, and service life. Despite these developments, several inherent limitations persist, primarily due to the nature of direct mechanical contact between meshing gear teeth. This contact leads to various tribological and mechanical issues, including adhesive wear, surface fatigue (pitting), crack propagation, and plastic deformation of gear teeth. In addition, gear meshing induces undesirable dynamic effects such as vibration, friction losses, and acoustic noise, while lubrication systems introduce further challenges such as leakage and maintenance requirements [1, 2].

Magnetic gears (MGs) have emerged as a highly promising alternative for torque transmission, leveraging non-contact magnetic coupling to overcome the fundamental limitations of conventional mechanical gears. Their operating principle is based on the interaction of synchronized magnetic fields, eliminating direct mechanical contact between rotating components.

This distinctive feature provides significant performance advantages. The absence of physical contact removes the primary source of frictional wear, thereby minimizing material degradation and substantially extending service life. Consequently, maintenance requirements, including lubrication and component replacement, are greatly reduced. In addition, the contactless transmission mechanism inherently suppresses vibration and acoustic noise, enabling smoother and quieter operation [3, 4]. Owing to these advantages, MGs have attracted increasing attention in high-performance applications, including electric vehicle propulsion systems [5, 6], renewable energy technologies such as wind turbines [7, 8], and aerospace actuation systems [9], where efficiency, reliability, and low noise are critical requirements.

The concept of magnetic gearing dates back to the early 20th century. One of the earliest contributions was reported by Armstrong in 1901, who demonstrated a device capable of transmitting mechanical power through magnetic field interaction, thereby establishing the fundamental principle of contactless torque transmission [10]. Subsequent developments increased structural complexity. In 1913, Neuland introduced a design comprising two rotors with salient steel poles interacting with a stationary electromagnetic structure, representing an early approach to controlled magnetic coupling [11]. A significant milestone was achieved in 1941 when Faus patented a MG employing permanent magnets (PMs) for power transmission, laying the groundwork for modern MG technologies [12].

Despite these early innovations, MGs were not widely adopted in industrial applications due to their low torque density. This limitation was primarily attributed to suboptimal magnetic circuit design and the inferior magnetic properties of early magnet materials, including low coercivity and remanence [13, 14]. As a result, these systems were confined to niche applications. Renewed interest in magnetic gearing emerged in the late 20th century, driven primarily by breakthroughs in high-performance magnetic materials and advanced electromagnetic design techniques [15].

A major breakthrough in magnetic gearing technology was achieved in 2001 when K. Atallah and D. Howe introduced the coaxial magnetic gear (CMG) concept [16]. This topology utilizes harmonic magnetic field interaction between concentric permanent magnet (PM) rotors to enable efficient torque transmission. The resulting magnetic coupling inherently provides speed reduction and torque amplification, governed by a fixed gear ratio determined by the pole-pair combination of the inner and outer rotors.

In the early stages of CMG development, the primary research focus was on increasing torque density. To achieve this, efforts were directed toward optimizing magnetic circuit topology [17], employing high-energy-density magnetic materials such as rare-earth PMs [18, 19], and refining magnet arrangements [20, 21], all of which play critical roles in enhancing torque production capability. A review of recent literature indicates that most CMG designs rely heavily on rare-earth PMs [22]. This trend is driven by the necessity of achieving high torque density, which remains a key performance metric. However, this reliance has also introduced challenges related to material cost and supply chain dependency, motivating further research into alternative design strategies.

The use of rare-earth PMs significantly enhances the performance of MG systems. However, these advantages are accompanied by substantial practical challenges that hinder large-scale adoption. The primary concern is the high cost of rare-earth materials, particularly neodymium-iron-boron (NdFeB) magnets, compared to conventional alternatives such as ferrite or Alnico. This issue is further exacerbated by the volatility of raw material prices and the geopolitical constraints associated with rare-earth supply chains [23]. In addition, the limited natural availability of key elements, such as neodymium and dysprosium, and the environmentally intensive extraction and processing procedures introduce further barriers to sustainability and scalability. Collectively, these challenges significantly limit the economic feasibility of MG systems, particularly in applications where cost efficiency and supply security are critical considerations. Therefore, reducing the reliance on rare-earth materials has become a critical research direction in the design of next-generation MGs.

To address these challenges, significant research efforts have been directed toward the use of non-rare-earth permanent magnet materials. Among these alternatives, ferrite and Alnico magnets have received considerable attention due to their low cost and wide availability [24, 25].

One of the earliest studies proposing the use of ferrite magnets in radial-flux CMGs was reported in [26], marking a shift away from exclusive reliance on rare-earth materials. This approach demonstrated the feasibility of developing cost-effective MG systems using lower-performance magnetic materials. Subsequent research has focused on improving the performance of ferrite-based designs. For instance, [27] introduced a CMG with consequent-pole rotors employing ferrite magnets, achieving enhanced torque density and reduced PM volume through optimized magnetic field distribution. Following these developments, several studies have conducted comparative analyses between ferrite-based and rare-earth-based MGs [28–31]. These investigations consistently highlight a fundamental trade-off: while ferrite-based designs offer improved cost-effectiveness, they generally exhibit lower torque density compared to their rare-earth counterparts. This inherent trade-off has motivated the development of hybrid MG designs that combine rare-earth and non-rare-earth materials to achieve a balance between cost and performance.

To overcome the limitations of both rare-earth and ferrite-based designs, hybrid MGs have been proposed, combining the advantages of different magnet materials within a single structure. These designs exploit the high magnetic performance of rare-earth PMs alongside the low cost of ferrite magnets to achieve an improved balance between torque density and economic efficiency [32–36].

Several studies have explored various hybrid configurations. For example, [33] and [34] proposed optimized rotor topologies that reduce rare-earth material usage while maintaining high torque density. Similarly, [35] investigated hybrid arrangements with improved resistance to demagnetization, while [36] introduced a novel topology that enhances both torque performance and cogging torque characteristics. Overall, these studies demonstrate that hybrid MG designs provide a promising pathway for achieving high-performance and cost-effective solutions, although challenges remain in optimizing magnetic flux distribution and minimizing undesirable effects such as leakage flux and cogging torque. However, achieving an optimal trade-off between torque density, cost reduction, and cogging torque mitigation remains an open challenge.

This study proposes two novel radial-flux CMG configurations aimed at reducing the reliance on rare-earth PMs while maintaining high torque performance. In both designs, a hybrid magnet arrangement combining rare-earth and ferrite materials is implemented within the inner rotor using a series–parallel magnetic circuit structure. This configuration is designed to enhance magnetic flux utilization and achieve a more uniform flux distribution. To further improve performance, an advanced topology incorporating flux barriers and optimized magnet placement is introduced. These features contribute to reducing cogging torque and mitigating flux leakage, thereby enhancing overall efficiency and torque smoothness.

A comprehensive multi-objective optimization framework is employed using a genetic algorithm integrated with 2-D FEA in ANSYS Maxwell. The optimization simultaneously targets output torque, cogging torque minimization, and reduction of permanent magnet volume, enabling a balanced trade-off between performance and cost. The effectiveness of the proposed designs is validated through detailed electromagnetic analysis and experimental investigations. The results confirm that the advanced configuration achieves improved performance compared to the conventional benchmark design.

2. Operating Principle

The proposed CMG operates based on magnetic field modulation produced by ferromagnetic pole pieces positioned between the inner and outer rotors. The inner and outer rotors are equipped with PMs having different pole-pair numbers, while the stationary modulation ring modifies the spatial distribution of the magnetic fields to establish synchronous torque transmission (Fig. 1).

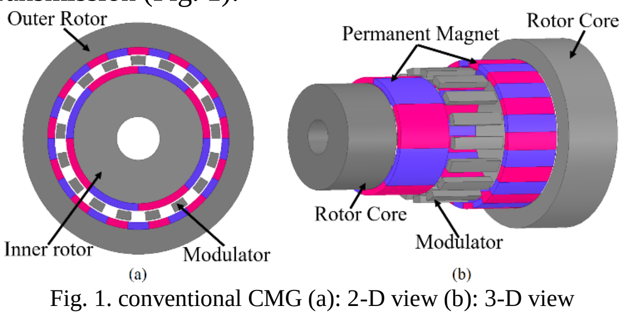

Fig. 1. conventional CMG (a): 2-D view (b): 3-D view

When the magnetic field generated by one rotor passes through the modulation ring, multiple spatial harmonic components are produced. Among these harmonics, specific components satisfy the synchronous condition required for effective magnetic coupling between the two rotors [37-39]. The relationship between the number of ferromagnetic pole pieces and the rotor pole-pair numbers is expressed as:

$$P_{inner} \pm P_{outer} = Q_{modulator} \quad (1)$$

where $Q_{modulator}$ is the number of ferromagnetic segments, and P_{inner} and P_{outer} denote the pole-pair numbers of the inner and outer rotors, respectively. Based on the harmonic interaction principle, the transmission gear ratio of the CMG is determined by (Fig. 2):

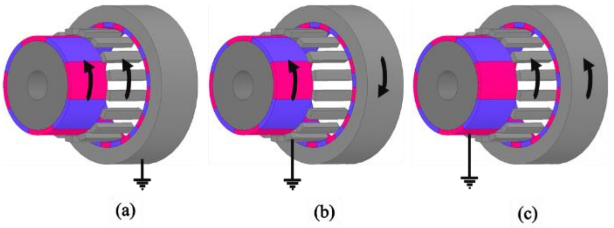

Fig. 2. Different operating modes of the MG and how the input and output rotors rotate (a) an outer rotor fixed, (b) modulator segments (pole pieces) fixed, and (c) inner rotor fixed

when the outer rotor is held stationary can be given by

$$G_r = +\frac{Q_{modulator}}{P_{inner}} \quad (2)$$

The gear ratio when the modulators are held stationary can be given by

$$G_r = -\frac{P_{outer}}{P_{inner}} \quad (3)$$

When the inner rotor is kept stationary, the gear ratio can be given by

$$G_r = +\frac{Q_{modulator}}{P_{outer}} \quad (4)$$

where the negative sign indicates opposite rotational directions of the two rotors. The electromagnetic torque is generated through the interaction of the dominant modulated harmonic fields. Compared with conventional mechanical gears, the proposed CMG achieves contactless torque transmission, resulting in reduced mechanical wear, lower maintenance requirements, and smoother operation. In the proposed topology, the hybrid rare-earth/ferrite magnet arrangement further improves magnetic flux utilization while reducing the dependency on rare-earth PM materials.

3. Hybrid Inner Rotor Design

Recent advancements in CMGs have primarily focused on optimizing the permanent magnet (PM) arrangement within the inner rotor to enhance torque performance and reduce undesirable torque components. Current research efforts aim to simultaneously maximize torque density and minimize cogging torque, which is a major source of torque ripple, vibration, and acoustic noise [34–41].

Among the various PM configurations, Arc-type [42], V-type [43], and Spoke-type [44] topologies are the most widely investigated. Spoke-type configurations exhibit a strong flux-focusing effect, resulting in higher magnetic flux concentration and superior torque density compared to V-type arrangements. However, this advantage is accompanied by increased cogging torque due to stronger magnetic interactions between the rotor magnets. In contrast, V-type topologies provide a more sinusoidal air-gap flux distribution, leading to smoother torque characteristics and reduced cogging torque [43, 44].

To achieve a balanced trade-off between torque density and torque quality, a novel asymmetric PM rotor topology is proposed in this study. The proposed configuration combines the flux-focusing capability of spoke-type arrangements with the improved torque smoothness of V-type structures. In addition, this study aims to reduce the dependency on rare-earth PM materials through a hybrid magnet configuration employing both rare-earth and ferrite magnets within the inner rotor. The magnetic performance of the proposed topology is strongly influenced by the magnetic circuit structure and the spatial arrangement of the PMs. Based on the magnetic flux path characteristics, the rotor configurations can generally be classified into series, parallel, and series–parallel magnetic circuits. Fig. 3 illustrates representative rotor structures corresponding to these magnetic circuit topologies.

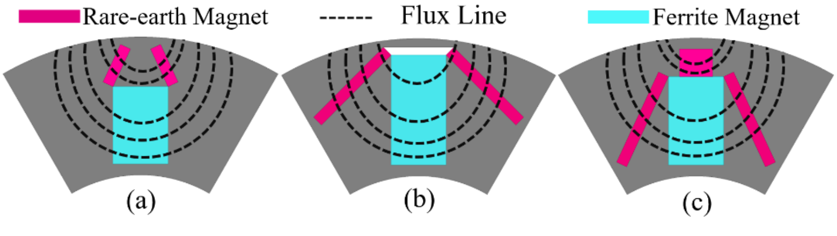

Fig. 3. Feasible rotor unit designs: (a) parallel magnetic circuit (b) series magnetic circuit, and (c) series-parallel magnetic circuit.

The series–parallel magnetic circuit configuration provides several advantages over conventional series or parallel arrangements in permanent magnet (PM) systems. By combining the characteristics of both topologies, the series–parallel structure achieves an improved balance between magnetic flux concentration, flux uniformity, and operational stability. In addition, the presence of multiple flux paths enhances resistance to self-demagnetization and improves magnetic field robustness under external disturbances and thermal conditions [45]. From an efficiency perspective, the optimized magnetic flux distribution of the series–parallel topology contributes to reduced magnetic losses and improved thermal performance, resulting in enhanced operational reliability. Owing to these advantages, the series–parallel magnetic circuit is considered a promising approach for high-performance CMG applications.

Based on this concept, this study proposes a novel hybrid magnetic architecture employing both rare-earth and ferrite PMs within a series–parallel magnetic circuit. The proposed design simultaneously targets three key objectives: high torque density, reduced cogging torque, and lower material cost. Fig. 4 illustrates the proposed dual-PM rotor configuration, which integrates NdFeB and ferrite magnets within a unified rotor structure. The proposed topology combines spoke-type and V-type magnet arrangements to exploit the flux-focusing capability of spoke-type structures while maintaining the smoother torque characteristics of V-type configurations.

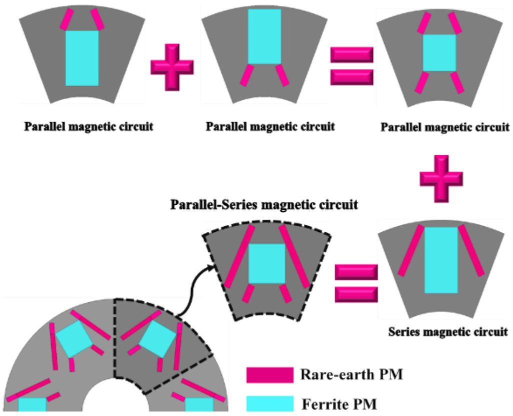

Fig. 4. Proposed hybrid inner rotor topology incorporating spoke-type ferrite and V-type rare-earth magnet arrangements within a series-parallel magnetic circuit.

As illustrated in Fig. 4, the proposed inner rotor employs a hybrid PM configuration consisting of one ferrite magnet and six rare-earth magnet segments. The ferrite magnet is positioned in a spoke-type arrangement to enhance magnetic flux concentration within the air gap, thereby improving torque density.

To optimize the magnetic circuit performance, the rare-earth magnets are arranged in both V-type and spoke-assisted configurations. Two rare-earth magnets are positioned above the ferrite magnet in a V-type structure, forming a parallel magnetic branch that improves flux control and reduces magnetic leakage. A symmetrical arrangement is implemented beneath the ferrite magnet to maintain magnetic field balance. In addition, two lateral rare-earth magnet segments establish a series magnetic path, reinforcing the magnetic flux generated by the ferrite magnet and increasing the overall magnetic field intensity. The resulting series–parallel magnetic circuit enhances magnetic flux utilization while improving resistance to demagnetization. Furthermore, the hybrid arrangement increases the operational effectiveness of the ferrite magnet, enabling reduced rare-earth material usage without significant degradation in torque performance. The initial configuration of the proposed hybrid CMG topology is illustrated in Fig. 5.

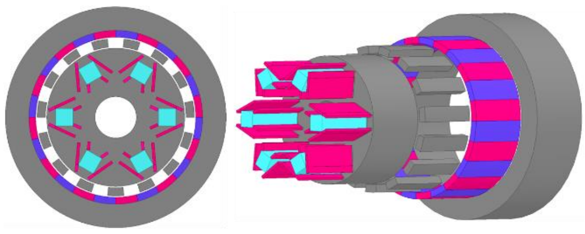

(a) (b)

Fig. 5. initial model of the proposed CMG: (a): 2-D view (b): 3-D exploded view

A critical limitation of the initial rotor configuration shown in Fig. 5 is the presence of considerable leakage flux within the inner rotor, which negatively affects torque density and magnetic field quality. In addition, achieving a near-sinusoidal air-gap flux distribution remains an important objective for reducing torque ripple and improving torque smoothness. Although the implemented V-type arrangement partially improves flux distribution, leakage flux remains significant.

To address these issues, flux barriers are incorporated into the inner rotor structure. These non-magnetic regions are strategically designed to suppress leakage flux and improve the air-gap magnetic flux distribution. The resulting rotor configuration after the introduction of flux barriers is illustrated in Fig. 6.

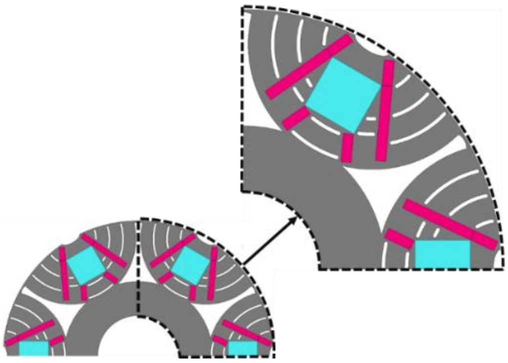

Fig. 6. Internal rotor of CMG with flux barriers

As shown in Fig. 7, fourteen flux barriers are integrated into the proposed inner rotor, resulting in the advanced CMG model. The combined implementation of the hybrid PM arrangement and flux barriers enhances magnetic flux guidance and improves the overall electromagnetic performance of the proposed structure. In the advanced model, most rotor zones are designed to guide and concentrate magnetic flux generated by both ferrite and rare-earth PMs. In contrast, specific regions operate as flux barriers to suppress internal leakage flux and prevent undesirable magnetic short-circuit paths between adjacent magnets. Consequently, a greater portion of the magnetic flux is directed toward the working air gap, contributing to improved torque transmission capability.

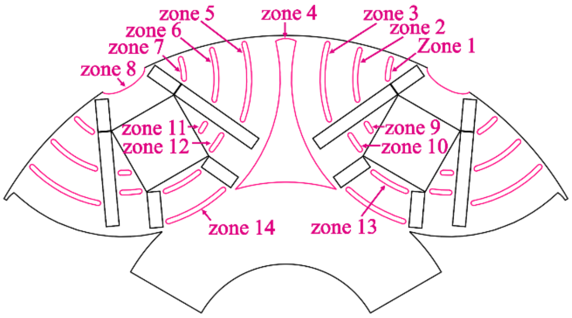

Fig. 7. Advanced rotor configuration with integrated flux barriers and functional magnetic flux guidance regions.

The final configuration, referred to hereafter as the advanced structure, is selected as the proposed CMG topology investigated in this study. All subsequent electromagnetic and mechanical analyses are conducted based on this structure. The initial configuration is considered as the benchmark model, and a comprehensive comparison between the two topologies is presented in the following sections.

4. Multi-objective Optimization and Electromagnetic Performance Analysis

4-1- Optimization framework

This paper proposes a novel CMG topology featuring a redesigned hybrid inner rotor. The proposed structure employs a combined arrangement of rare-earth (NdFeB) and ferrite PMs, as illustrated in Fig. 8(b), to improve magnetic flux distribution and enhance torque transmission capability. In addition, fourteen asymmetrically distributed flux barriers are incorporated into the rotor core to suppress leakage flux, reduce cogging torque, and improve magnetic flux guidance toward the working air gap.

The combined implementation of the hybrid PM arrangement and flux barriers provides an effective trade-off between output torque, operational smoothness, and material cost. Compared with conventional single-material rotor structures, the proposed topology achieves improved electromagnetic performance while reducing rare-earth PM volume and cost-equivalent PM volume. To ensure a fair evaluation, both the benchmark model (initial structure) and the advanced model (proposed structure with flux barriers) are optimized under the same optimization framework and using consistent GA settings. The optimization process determines the optimal design parameters for each topology based on the defined objective functions. Subsequently, the optimized models are comparatively evaluated to identify the impact of the proposed structural modifications on the electromagnetic and mechanical performance of the CMG. The parameterized geometries of the benchmark and advanced models are shown in Fig. 8, while the corresponding design parameters are summarized in Table 1.

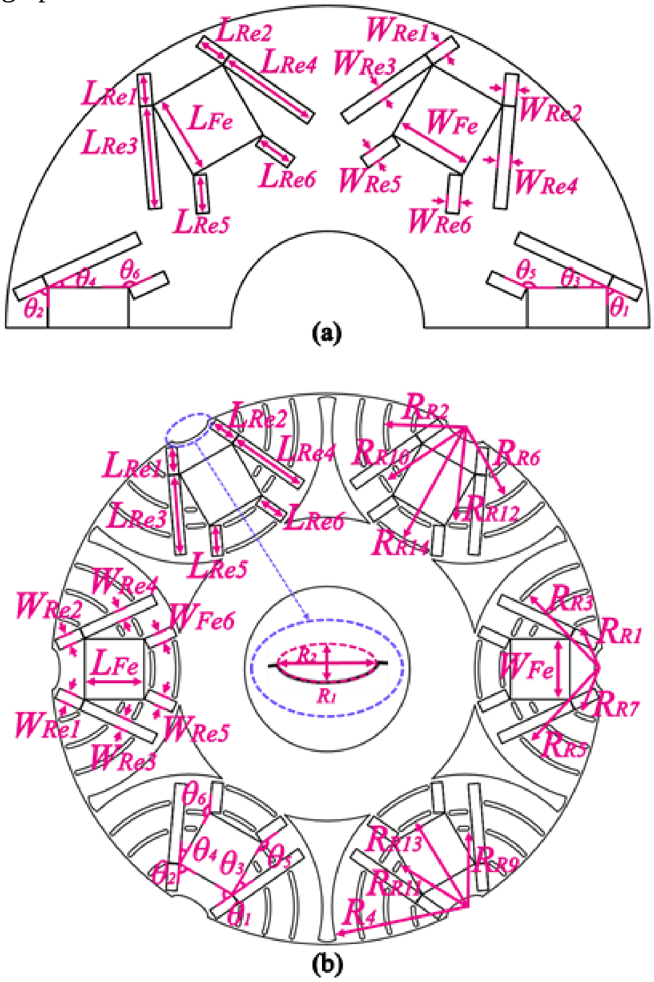

Fig. 8. Optimization parameters of inner rotor (a) benchmark structure. (b) advanced structure

Table 1. Initial design parameters of hybrid PM CMG

Parameter	Symbol	Benchmark model Value	Advanced model Value
Number of internal rotor pole pairs	P_{inner}	3	3
Number of outer rotor pole pairs	P_{outer}	12	12
Number of ferromagnetic pole pieces – M400	$Q_{modulator}$	15	15
Inner radius	R_{shaft}	15 mm	15 mm
Radial length of low-speed PMs	L_{PM}	5 mm	5 mm
Radial length of Each air gap	L_g	1 mm	1 mm
Radial length of ferromagnetic pole pieces	L_M	6 mm	6 mm
Effective Radial length of high-speed core – M400	R_{in}	50 mm	50 mm
Effective Radial length of outer rotor	R_{out}	80 mm	80 mm
Effective Radial thickness of outer core – M400	------	17 mm	50 mm
Slot opening of ferromagnetic pole-pieces	------	12 deg	12 deg
Width of the ferrite PMs	L_{Fe}	10 mm	10 mm
Thickness of the ferrite PMs	W_{Fe}	10 mm	10 mm
Width of the rare-earth PMs in the parallel branch	L_{Re1}	4 mm	4 mm
Thickness of the rare-earth PMs in the parallel branch	W_{Re1}	2 mm	2 mm
Width of the rare-earth PMs in the parallel branch	L_{Re2}	4 mm	4 mm
Thickness of the rare-earth PMs in the parallel branch	W_{Re2}	2 mm	2 mm

Width of the rare-earth PMs in the series branch	L_{Re3}	*14 mm*	*14 mm*
Thickness of the rare-earth PMs in the series branch	W_{Re3}	*2 mm*	*2 mm*
Width of the rare-earth PMs in the series branch	L_{Re4}	*14 mm*	*14 mm*
Thickness of the rare-earth PMs in the series branch	W_{Re4}	*2 mm*	*2 mm*
Width of the rare-earth PMs in the parallel branch	L_{Re5}	*4 mm*	*4 mm*
Thickness of the rare-earth PMs in the parallel branch	W_{Re5}	*2 mm*	*2 mm*
Width of the rare-earth PMs in the parallel branch	L_{Re6}	*4 mm*	*4 mm*
Thickness of the rare-earth PMs in the parallel branch	W_{Re6}	*2 mm*	*2 mm*
Angle between rare-earth PM and ferrite	θ_1	*25 deg*	*25 deg*
Angle between rare-earth PM and ferrite	θ_2	*25 deg*	*25 deg*
Angle between rare-earth PM and ferrite	θ_3	*25 deg*	*25 deg*
Angle between rare-earth PM and ferrite	θ_4	*25 deg*	*25 deg*
Angle between rare-earth PM and ferrite	θ_5	*140 deg*	*140 deg*
Angle between rare-earth PM and ferrite	θ_6	*140 deg*	*140 deg*
Radius of zone 1	R_{R1}	------	*8 mm*
Radius of zone 2	R_{R2}	------	*17 mm*
Radius of zone 3	R_{R3}	------	*18.5 mm*
Radius of zone 4	R_{R4}	------	*23 mm*
Radius of zone 5	R_{R5}	------	*18.5 mm*
Radius of zone 6	R_{R6}	------	*17 mm*
Radius of zone 7	R_{R7}	------	*8 mm*
Small diameter of zone 8	R_1	------	*2 mm*
Large diameter of zone 8	R_2	------	*7 mm*
Radius of zone 9	R_{R9}	------	*14 mm*
Radius of zone 10	R_{R10}	------	*17 mm*
Radius of zone 11	R_{R11}	------	*14 mm*
Radius of zone 12	R_{R12}	------	*17 mm*
Radius of zone 13	R_{R13}	------	*17 mm*
Radius of zone 14	R_{R14}	------	*20 mm*
Total height	------	*50 mm*	*50 mm*

4-2- Objective Functions and Optimization Constraints

The first stage of the optimization process involves identifying the key design parameters of the proposed CMG. Since the main objectives are to maximize output torque, minimize cogging torque, and reduce final cost, the optimization variables are selected from the inner rotor geometry, which has the greatest influence on the electromagnetic performance of the structure. As shown in Fig. 8, the benchmark model includes 20 independent design parameters associated with the PM geometry and arrangement, including the dimensions and angular positions of the magnets employed in the V-type configuration. In the advanced model, 15 additional parameters related to the flux barrier geometry are introduced, resulting in a total of 35 optimization variables. The PM volume primarily affects torque capability and material cost, while the magnet arrangement and flux barrier geometry strongly influence cogging torque characteristics. Therefore, all geometric parameters shown in Fig. 8 are considered as optimization variables.

The second stage of the optimization framework is the selection of an appropriate optimization algorithm. Conventional gradient-based optimization methods often exhibit limited performance in high-dimensional and non-convex design spaces due to their tendency to converge toward local optima. To overcome these limitations, meta-heuristic optimization approaches have been widely adopted [46-48]. Among them, Genetic Algorithms (GAs) provide an effective optimization framework for complex electromagnetic systems because of their strong global search capability and robustness in multi-modal search spaces.

In the GA process, an initial population of candidate solutions is generated and evaluated using the defined objective function. The optimization procedure iteratively updates the population through selection, crossover, and mutation operators to improve the fitness of the candidate solutions. This evolutionary process continues until the termination criterion is satisfied [49-51].

In the third stage, a multi-objective function is defined to simultaneously maximize the average output torque while minimizing cogging torque and total material cost. Since PMs constitute the dominant cost component of the CMG, the optimization process considers the total PM volume as the primary cost-related parameter. To account for the cost difference between ferrite and rare-earth magnets, a weighting factor is introduced in the objective function. Based on [52], rare-earth PMs are assumed to be approximately 15 times more expensive than ferrite magnets per unit volume. Accordingly, the ferrite PM volume is scaled using this factor to obtain a cost-equivalent magnetic material volume for the optimization process.

According to the described optimization framework, the proposed CMG is optimized based on the following objective function:

$$f_{max}(s_i) = \lambda_1 \frac{T_{(s_i)}}{T_{(initial)}} + \lambda_2 \frac{PM\ volume_{\ (initial)}}{PM\ volume_{(s_i)}} + \lambda_3 \frac{T_{cogging\,(initial)}}{T_{cogging\,(s_i)}} \quad (10)$$

$$PM_{volume} = PM_{volume_{Nd}} + \frac{PM_{volume_{Fe}}}{15} \quad (11)$$

$$T_{cogging} = \frac{T_{max} - T_{min}}{T_{avg}} \quad (12)$$

$$\lambda_1 + \lambda_2 + \lambda_3 = 1 \quad (13)$$

Equation (10) incorporates the reference values of the inner rotor torque ($T_{(initial)}$), cogging torque ($T_{cogging_{(initial)}}$), and PM volume ($PM\ volume_{(initial)}$). The corresponding optimized quantities, namely $T_{(s_i)}$, $T_{cogging_{(s_i)}}$, and $PM\ volume_{(s_i)}$ are functions of the design variabless_i. The weighting coefficients λ_1, λ_2, and λ_3 determine the relative contributions of torque, PM volume, and cogging torque within the optimization framework. As defined in Eq. (11), the total PM volume is calculated from the combined volumes of the rare-earth and ferrite magnets. To account for the cost difference between the two materials, the ferrite PM volume is normalized using a weighting factor of 15, yielding a cost-equivalent magnetic material volume. In addition, the cogging torque term in Eq. (12) is defined as the ratio of peak-to-peak torque to the average torque value.

The weighting coefficients λ_1, λ_2, and λ_3 in (13) are assigned equal values, i.e., $\lambda_1 = \lambda_2 = \lambda_3 = \frac{1}{3}$, to provide equal importance to the three considered objectives: torque, permanent-magnet volume, and cogging torque. This choice avoids introducing a preferential weighting among the competing objectives and provides a balanced optimization criterion. The objective functions are normalized before their combination to eliminate the effect of differences in numerical scale and physical units. Consequently, the selected weighting coefficients enable the optimization to identify Pareto-optimal solutions that provide a balanced tradeoff among electromagnetic performance, permanent-magnet utilization, and cogging-torque reduction.

After defining the optimization variables, optimization algorithm, and objective function, the proposed CMG is optimized using the FEM software environment. During the optimization process, the GA iteratively generates candidate parameter sets, performs electromagnetic simulations, and evaluates the resulting torque, cogging torque, and PM volume values using the defined objective function. The optimization loop continues until the convergence criteria are satisfied. The overall optimization procedure is illustrated in Fig. 9.

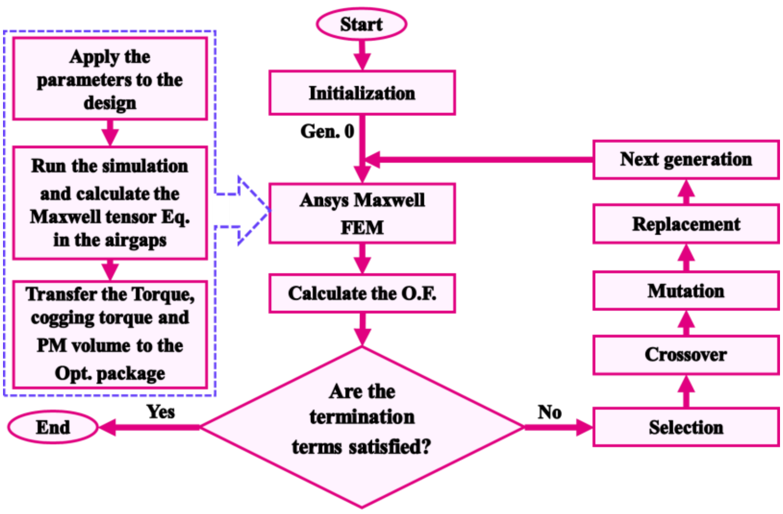

Fig.9. Optimization process

4-3- Pareto Optimization Results

The genetic algorithm settings adopted for the multi-objective optimization of the benchmark and advanced CMG configurations are summarized in Table 2. The initial population size is selected based on the dimensionality of the corresponding design space, with the initial number of candidate solutions set to ten times the number of optimization variables. This criterion provides a sufficiently diverse initial population while maintaining a reasonable computational burden for the subsequent FEM-based evaluations. The number of samples evaluated per iteration determines the number of candidate solutions considered during each optimization iteration. The crossover probability specifies the likelihood of generating new candidate solutions through the recombination of selected parent solutions, whereas the mutation probability controls the introduction of random variations in the optimization variables to preserve population diversity and exploration of the design space. The maximum number of iterations defines the upper limit of the optimization process, while the maximum allowable Pareto percentage determines the permitted proportion of non-dominated solutions within the population. The convergence stability percentage is employed as a termination criterion to identify a sufficiently stable optimization state. Accordingly, the initial population sizes are set to 200 and 350 for the benchmark and advanced configurations, respectively, while 100 and 170 samples are evaluated per iteration. The crossover and mutation probabilities are set to 0.9 and 0.05, respectively. The maximum numbers of iterations are 45 and 65 for the benchmark and advanced configurations, respectively. The maximum allowable Pareto percentage and convergence stability percentage are set to 75% and 15%, respectively. These settings establish the computational framework and termination criteria for the GA-based multi-objective optimization.

Table 2. Optimization settings of hybrid PM CMG

Optimization algorithm settings	***Benchmark model***	***Advanced model***
Initial sample number	200	350
Samples per iteration number	100	170
Probability of crossover	0.9	0.9
Probability of mutation	0.05	0.05
Maximum iterations	45	65
Maximum allowable Pareto percentage	75	75
Convergence stability percentage	15	15

Fig. 10 illustrates the Pareto-optimal frontier obtained from the multi-objective optimization process. Each point on the frontier represents a non-dominated solution in which improvement of one objective function leads to degradation in at least one of the remaining objectives. Therefore, the Pareto front provides a set of optimal trade-off solutions rather than a single global optimum.

It should be noted that the proposed CMG is intended for a 1-kW wind energy conversion system in which the wind-turbine rotor operates at a maximum speed of 200 rpm, while the generator is required to operate at up to 1000 rpm. Accordingly, a 5:1 transmission ratio is adopted to provide the required speed matching between the low- and high-speed sides. Such an operating-speed combination is also consistent with magnetic-gear design studies, in which a 5:1 ratio is employed to convert 1000-rpm high-speed operation to 200-rpm low-speed operation [53]. At the rated power of 1 kW, the corresponding torque requirement at the 1000-rpm high-speed rotor is 9.55 Nm. These application-driven operating conditions are therefore established as the basis for evaluating the torque-transmission capability and practical suitability of the optimized CMG configurations.

To enable a fair comparison between the benchmark and Advanced CMG models, one candidate solution is selected from the Pareto frontier such that both topologies provide approximately the required torque in the 2-D optimization stage, with the Advanced configuration reaching 9.55 Nm at the high-speed rotor. The corresponding optimized design parameters of the selected configurations are summarized in Table 3. This selection criterion establishes a consistent performance basis for evaluating secondary characteristics, including cogging torque, PM volume, losses, and efficiency. The selected configurations are subsequently evaluated using both 2-D and 3-D finite-element simulations based on the optimized design parameters listed in Table 3. The 3-D FEA results show lower torque values than the corresponding 2-D results because of axial leakage flux and end effects that are not represented in the 2-D model. Accordingly, the 9.55 Nm value represents the application-driven torque target used during the optimization and candidate-selection stage, whereas the lower 3-D torque values reported in Table 4 represent the final three-dimensional electromagnetic performance of the selected configurations.

It is worth noting that the upper and lower bounds of the optimization variables listed in Table 3 are defined based on the feasible geometric design space of the inner rotor. Since the optimization variables directly determine the dimensions, positions, and angular distributions of the permanent magnets and flux-barrier regions, their allowable ranges must satisfy both electromagnetic and geometrical requirements. Accordingly, the limits are established by considering the initial rotor geometry, the available radial and circumferential space, the required separation between adjacent magnetic components, and the preservation of sufficient structural material between the permanent magnets and the rotor boundaries. For the permanent-magnet-related parameters, the prescribed ranges are selected such that the magnets remain completely confined within their designated rotor regions and maintain physically feasible dimensions throughout the optimization process. The corresponding angular parameters are bounded to prevent excessive overlap, interference, or geometrically invalid magnet arrangements. For the flux-barrier parameters introduced in the advanced configuration, the allowable ranges are determined according to the available rotor-core space and the required magnetic and mechanical separation between adjacent regions. These bounds ensure that the flux barriers remain fully embedded within the rotor core without intersecting the permanent magnets, rotor boundaries, or neighboring barriers.

In addition to these geometric considerations, the parameter ranges are restricted to practically realizable configurations and are selected around the initial design to avoid generating solutions with excessively small or large geometric features that would be impractical to manufacture or would result in physically unrealistic rotor configurations. Thus, the optimization domain is defined as a feasible engineering design space rather than an unrestricted mathematical search space. This approach prevents the genetic algorithm from evaluating infeasible geometries and ensures that the obtained Pareto-optimal solutions correspond to physically realizable CMG configurations.

ultimate choice

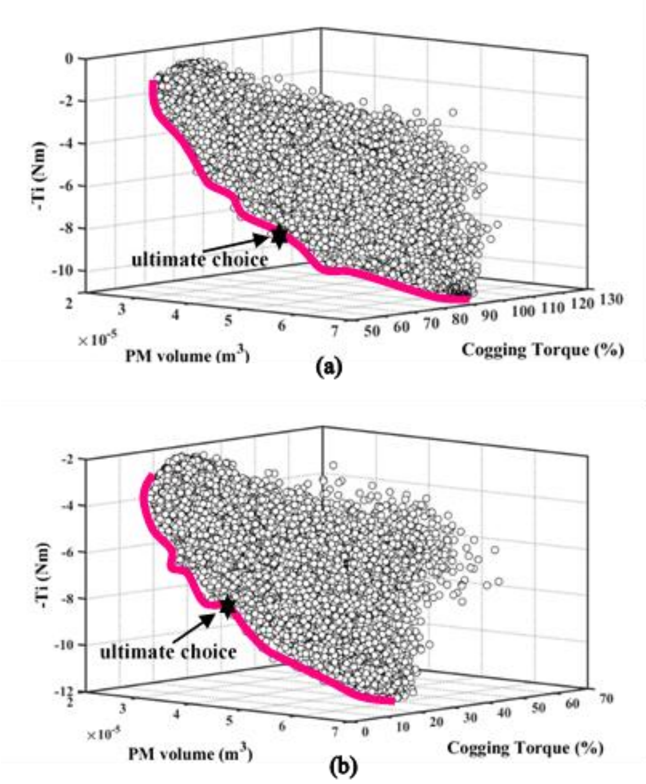

Fig. 10. Multi-objective optimization results pareto front for the proposed CMG: (a) benchmark structure and (b) advanced structure

Table 3. Optimization results of hybrid PM CMG

Optimization variable (Symbol)	*Min.*	*Max.*	*Optimal value*	
			Benchmark model	***Advanced model***
L_{Fe}	*10 mm*	*15 mm*	*14.9 mm*	*10.2 mm*
L_{Re1}	*4 mm*	*6 mm*	*4.3 mm*	*4.8 mm*
L_{Re2}	*4 mm*	*6 mm*	*5.8 mm*	*4.7 mm*
L_{Re3}	*13 mm*	*15 mm*	*14.7 mm*	*14.8 mm*
L_{Re4}	*13 mm*	*15 mm*	*14.9 mm*	*14.7 mm*
L_{Re5}	*6 mm*	*8 mm*	*7.6 mm*	*6 mm*
L_{Re6}	*6 mm*	*8 mm*	*7.8 mm*	*6.2 mm*
W_{Fe}	*10 mm*	*15 mm*	*14.8 mm*	*10.5 mm*

W_{Re1}	*1 mm*	*3 mm*	*1.8 mm*	*1.7 mm*
W_{Re2}	*1 mm*	*3 mm*	*1.9 mm*	*1.9 mm*
W_{Re3}	*2 mm*	*4 mm*	*3.9 mm*	*3 mm*
W_{Re4}	*2 mm*	*4 mm*	*3.8 mm*	*3.2 mm*
W_{Re5}	*2 mm*	*4 mm*	*2 mm*	*3.4 mm*
W_{Re6}	*2 mm*	*4 mm*	*2.3 mm*	*2.6 mm*
θ_1	*30 deg*	*45 deg*	*31.7 deg*	*38.1 deg*
θ_2	*30 deg*	*45 deg*	*36.4 deg*	*42.7 deg*
θ_3	*15 deg*	*30 deg*	*29.9 deg*	*24.2 deg*
θ_4	*15 deg*	*30 deg*	*27.4 deg*	*28.3 deg*
θ_5	*135 deg*	*165 deg*	*135.4 deg*	*137.2 deg*
θ_6	*135 deg*	*165 deg*	*136.1 deg*	*157.2 deg*
R_1	*1 mm*	*4 mm*	------	*3.2 mm*
R_2	*6 mm*	*10 mm*	------	*7.5 mm*
R_{R1}	*6 mm*	*10 mm*	------	*8.6 mm*
R_{R2}	*12 mm*	*16 mm*	------	*15.9 mm*
R_{R3}	*17 mm*	*20 mm*	------	*18.4 mm*
R_{R4}	*21 mm*	*25 mm*	------	*23.7 mm*
R_{R5}	*17 mm*	*20 mm*	------	*19 mm*
R_{R6}	*12 mm*	*16 mm*	------	*14.1 mm*
R_{R7}	*6 mm*	*10 mm*	------	*8.3 mm*
R_{R9}	*13 mm*	*15 mm*	------	*13.4 mm*
R_{R10}	*16 mm*	*18 mm*	------	*16.3 mm*
R_{R11}	*13 mm*	*15 mm*	------	*13.5 mm*
R_{R12}	*16 mm*	*18 mm*	------	*16.6 mm*
R_{R13}	*17 mm*	*20 mm*	------	*17.2 mm*
R_{R14}	*21 mm*	*24 mm*	------	*23.8 mm*

4-4- Electromagnetic Performance Comparison

Figures 11 and 12 compare the static and dynamic performances of the optimized benchmark and advanced CMG models for the high-speed and low-speed rotors, respectively. The torque, cogging torque, and PM volume of the benchmark and advanced CMG models are compared in Table 4.

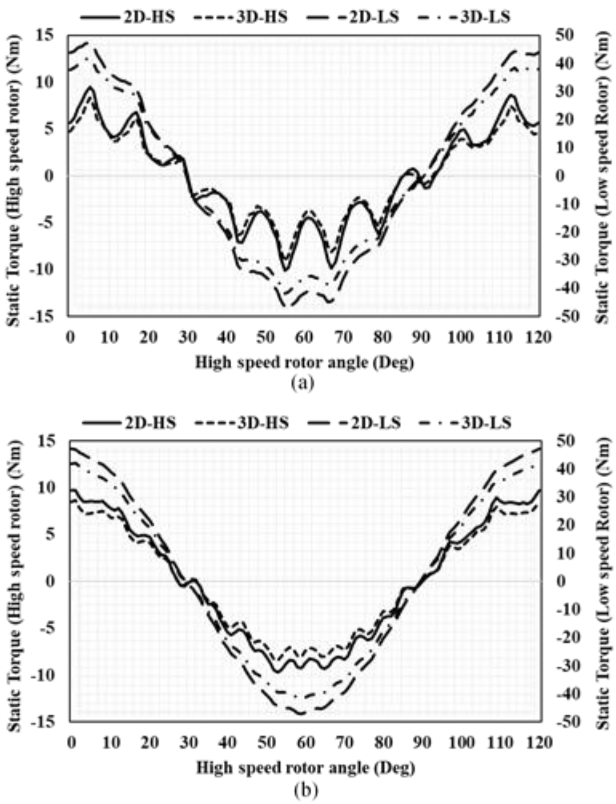

Fig. 11. Static Torque of middle rotor (LS) and inner rotor (HS) of optimal MG using 2-D and 3-D FEM: (a) benchmark structure (b) advanced structure

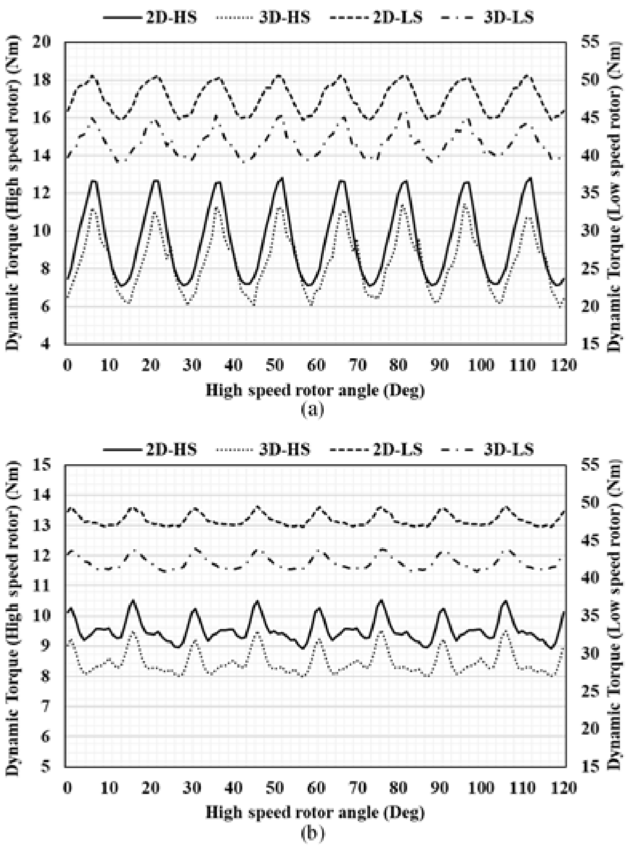

Fig. 12. Dynamic Torque of middle rotor (LS) and inner rotor (HS) of optimal MG using 2-D and 3-D FEM: (a) benchmark structure (b) advanced structure

Table 4. Optimal output performances of hybrid PM CMG.

		Benchmark model		Advanced model	
		2-D FEM	3-D FEM	2-D FEM	3-D FEM
high speed rotor	T_{avg} (Nm)	9.51	8.29	9.55	8.48
	T_{cog} (%)	59.96	64.03	15.75	17.07
	TD (kNm/m^3)	9.46	8.24	9.5	8.43
	TPV (kNm/m^3)	175.78	153.23	209.43	185.96
	Ferrite PM_{volume} (m^3)	6.61×10^{-5}		3.21×10^{-5}	
	Rare-earth PM_{volume} (m^3)	4.97×10^{-5}		4.35×10^{-5}	
	Cost-equivalent PM_{volume} (m^3)	5.41×10^{-5}		4.56×10^{-5}	
	$TOTAL_{volume}$ (m^3)	1.0053×10^{-3}		1.0053×10^{-3}	
Low speed rotor	T_{avg} (Nm)	47.61	41.45	47.76	42.04
	T_{cog} (Nm)	12.42	16.78	5.09	7.12

A comparison between the 2-D and 3-D models reveals that the predicted torque values in the 3-D simulations are lower for both CMG topologies. For the advanced model, the inner rotor torque obtained from the 3-D analysis is 11.2% lower than the corresponding 2-D result, while the benchmark model exhibits a reduction of 12.82%. Similarly, the low-speed rotor torque decreases by 12.93% in the benchmark model and 11.97% in the advanced model when transitioning from 2-D to 3-D simulations. These differences are primarily attributed to the inclusion of end effects and leakage flux in the 3-D models, which are neglected in conventional 2-D simulations [54]. A further comparison of the optimized structures in Table 4 demonstrates that the advanced model achieves a significant reduction in cogging torque while maintaining nearly identical output torque. The 2-D FEM results show a 73.7% reduction in the cogging-torque index, while the corresponding 3-D FEM results indicate a reduction of approximately 73.3%. This improvement is mainly attributed to the implementation of flux barriers, which effectively guide the magnetic flux and suppress undesirable leakage paths within the inner rotor.

Torque density (TD) is a key performance index for MGs because it quantifies the torque-transmission capability relative to the active volume of the device. As indicated in Table 4, the TD of the Advanced configuration is very close to that of the benchmark configuration. This behavior is expected because both configurations are designed to produce the nearly identical output torque and have identical primary geometric dimensions, including the outer-rotor diameter, inner-rotor diameter, and core depth. Consequently, both the torque capability and active volume remain essentially unchanged, resulting in negligible variation in TD between the two configurations. However, conventional TD does not explicitly account for the amount of magnetic material required to achieve the desired torque capability. Therefore, it provides limited insight into the effectiveness of magnetic-material utilization, particularly when reducing permanent-magnet volume is a primary design objective. To overcome this limitation, the torque per cost-equivalent permanent-magnet volume (TPV) index is introduced as a complementary performance metric. TPV is defined as the ratio of the output torque to the cost-equivalent volume of permanent-magnet material incorporated in the inner rotor, thereby quantifying the torque capability achieved per unit volume of magnetic material. Unlike conventional TD, TPV directly reflects the effectiveness of permanent-magnet material utilization in torque transmission.

As reported in Table 4, the 3-D FEM results demonstrate that the TPV increases from 153.23 kNm/m^3 for the benchmark configuration to 185.96 kNm/m^3 for the Advanced configuration, yielding a 21.36% improvement. The corresponding 2-D FEM analysis predicts a higher improvement of approximately 19.14%. This difference is primarily attributable to 3-D electromagnetic phenomena, particularly axial leakage flux and end effects, which are inherently neglected in the 2-D FEM formulation. Nevertheless, both analyses consistently identify the same performance trend, with the Advanced configuration exhibiting a higher torque capability per unit volume of PM material than the benchmark configuration. These results further confirm the improved utilization of the PM material achieved by the Advanced configuration.

It is worth noting that the Advanced configuration introduces additional geometrical complexity into the inner rotor owing to the incorporation of flux barriers and the modified permanent-magnet (PM) arrangement, which may increase the manufacturing complexity compared with the benchmark configuration. However, this additional complexity is localized within the inner rotor and does not require any increase in the overall dimensions or active volume of the CMG. In return, the Advanced configuration provides notable electromagnetic and material-utilization benefits. Specifically, the cost-equivalent PM volume is reduced by 15.7% compared with the benchmark configuration, while the 2-D FEM results demonstrate a 73.7% reduction in cogging torque. This substantial reduction in cogging torque is achieved while maintaining a comparable average torque and essentially unchanged overall active volume. Therefore, the advanced topology offers a favorable trade-off between structural complexity, PM-material utilization, and electromagnetic performance, particularly when the reduction of PM-material consumption and improvement of torque quality are considered as key design objectives.

Figures 13 and 14 illustrate the magnetic flux line distributions and magnetic flux density distributions of the optimized CMG topologies, respectively. These results demonstrate the magnetic coupling characteristics of the advanced structures and verify the effectiveness of the flux-guidance strategy in reducing leakage flux and improving air-gap magnetic field distribution.

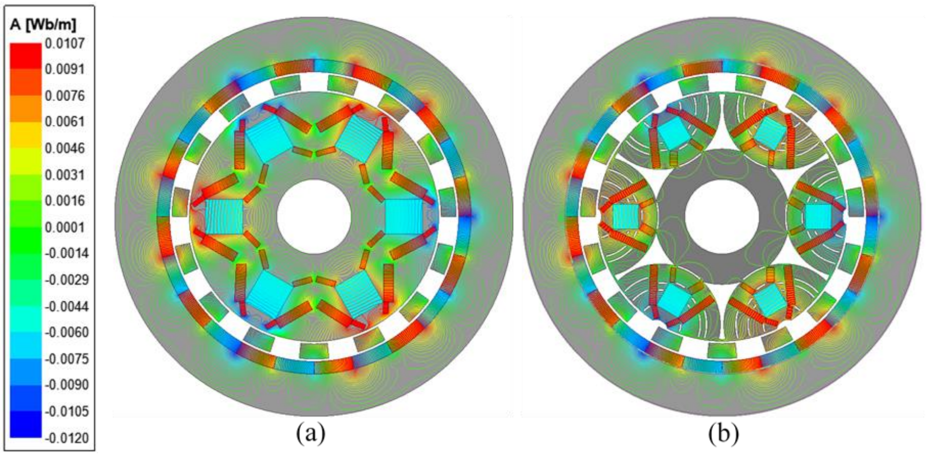

Fig.13. 2-D cross section view of magnetic vector potential lines distribution (a) benchmark structure. (b) advanced structure

A comparison of the magnetic vector potential flux line distributions in Fig. 13 reveals that the advanced CMG topology achieves improved magnetic flux guidance compared with the benchmark structure. In the advanced model, the integrated flux barriers effectively confine the magnetic flux within the desired paths, reducing leakage flux inside the inner rotor. As a result, stronger magnetic coupling is established between the rotating components, contributing to improved electromagnetic performance.

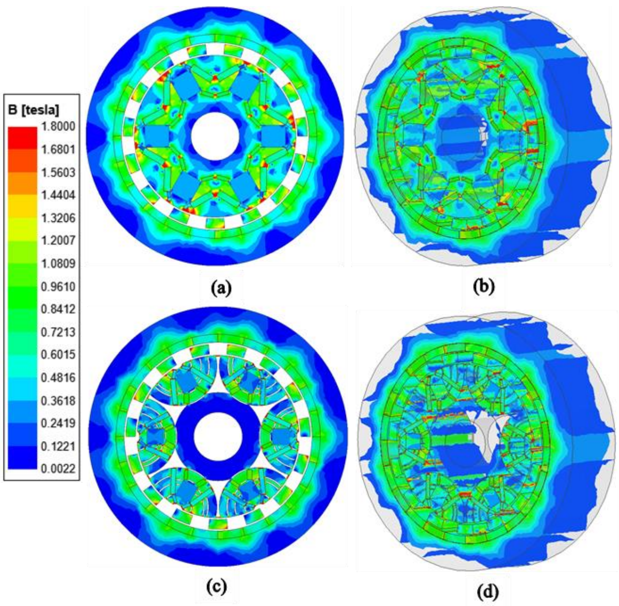

Fig.14. Flux density magnitude distribution: (a) 2-D view of benchmark structure (b) 3-D view of benchmark structure (c) 2-D view of advanced structure (d) 3-D view of advanced structure

The magnetic flux density distributions obtained from the 2-D and 3-D simulations in Fig. 14 further demonstrate the effectiveness of the proposed structure. Compared with the advanced model, the benchmark topology exhibits more extensive magnetic saturation regions, particularly in the areas between adjacent rare-earth magnets where the magnetic flux becomes highly concentrated. In contrast, the optimized flux-guidance structure of the advanced model improves magnetic flux distribution and reduces localized saturation effects.

4-5- Magnetic Flux and Harmonic Analysis

A further comparison is performed through the analysis of the air-gap magnetic flux density distributions, which strongly influence torque capability and electromagnetic losses. Fig. 15 presents the radial and tangential components of the air-gap magnetic flux density for both CMG topologies as a function of angular position. To evaluate the harmonic characteristics of the magnetic field, Fourier analysis is applied to the obtained waveforms. The corresponding harmonic spectra of the radial and tangential flux density components are illustrated in Fig. 16. These results provide a detailed assessment of the influence of the advanced topology on the harmonic behavior of the CMG magnetic field.

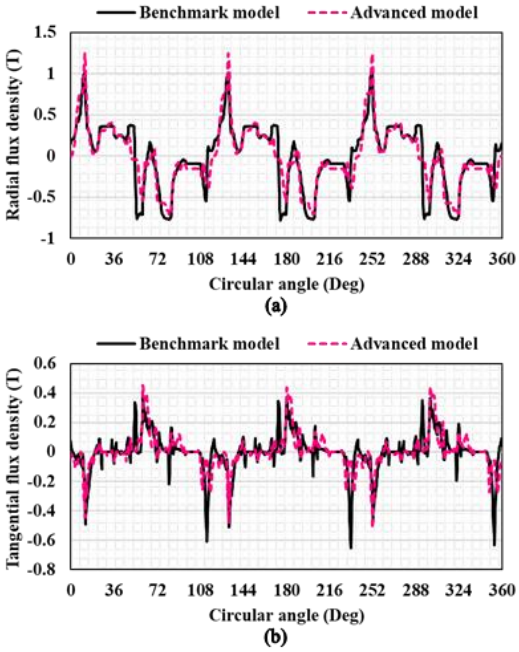

Fig.15. Flux density distribution in the inner air gap. (a) Radial component. (b) Tangential component.

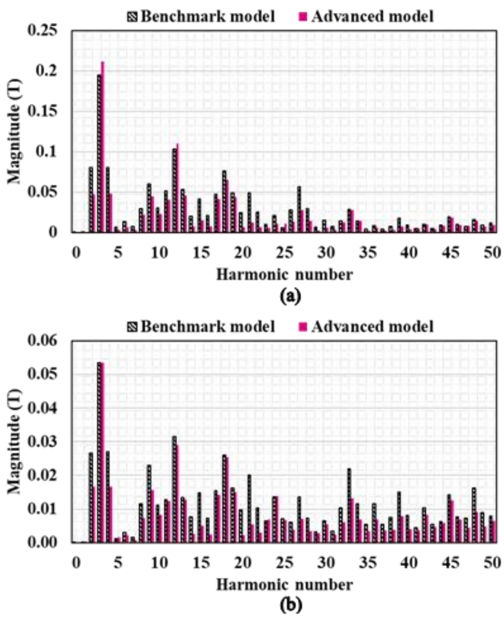

Fig.16. Harmonic spectra of flux density in the inner air gap. (a) Radial component. (b) Tangential component.

As illustrated in Fig. 16, the advanced CMG model significantly suppresses high-order harmonic components in both the radial and tangential magnetic flux density distributions. In particular, the amplitudes of the 14th, 21st, 33rd, 36th, 41st, and 44th harmonics are noticeably reduced. This attenuation is expected to contribute to smoother torque characteristics and reduced torque ripple. Furthermore, the attenuation of high-order harmonics decreases electromagnetic losses, particularly under high-speed operating conditions. Unlike conventional electric machines, MGs do not contain windings and therefore inherently eliminate copper losses. However, MGs are still subject to core losses, primarily consisting of eddy current and hysteresis losses. The eddy current losses in the PMs, denoted by W_{ec}, can be calculated using harmonic decomposition as follows [55]:

$$W_{ec} = \sum_{n=1}^{\infty} \int_{v} \frac{\left|J_{e,n}\right|^{2}}{2\sigma} dv \tag{14}$$

where $J_{e,n}$ is the eddy current density associated with the n^{th} harmonic component and \sigma is the electrical conductivity of the PM material. Similarly, the iron losses in the ferromagnetic components, including the inner rotor, outer rotor, and modulation ring, can be evaluated based on the harmonic components of the magnetic field using the following expression [56,57]:

$$W_{iron} = W_{hy} + W_{ec} = \sum_{n}^{\infty} \left\{ \int_{iron} \left[A_h k f ({B_{nr}}^2 + {B_{nt}}^2) + A_e (kf)^2 ({B_{nr}}^2 + {B_{nt}}^2) \right] dv \right\} \qquad (15)$$

In the presented formulation, W_{hy} and W_{ec} denote the hysteresis and eddy current losses in the silicon steel laminations, respectively. The excitation frequency is represented by f, while B_{nr} and B_{nt} correspond to the radial and tangential magnetic flux density components. The coefficients A_h and A_e represent the material-dependent hysteresis and eddy current loss coefficients of the silicon steel sheets.

Fig. 17 compares the hysteresis and eddy current losses of the benchmark and advanced CMG structures over a range of rotational speeds. At low rotational speeds, hysteresis losses dominate in both topologies. However, with increasing speed, eddy current losses increase significantly and become the dominant loss component due to their frequency-dependent behavior.

The advanced structure consistently exhibits lower hysteresis and eddy current losses compared with the benchmark model across the entire operating range. At 10000 rpm, for example, the hysteresis loss of the advanced structure is 13.71 W, whereas the benchmark structure exhibits 17.42 W, corresponding to a 27.06% increase. Similarly, the advanced model achieves an approximately 34.81% reduction in eddy current losses compared with the benchmark topology. Fig. 18 presents a comparative analysis of PM eddy current losses (solid losses) and core losses as functions of rotational speed. The results indicate that the advanced structure achieves lower losses in both categories throughout the investigated speed range. In addition, at high rotational speeds, the solid losses become significantly larger than the corresponding core losses in both configurations. The reduction in losses achieved by the advanced structure is mainly attributed to the suppression of high-order harmonic components, as demonstrated in Fig. 16, together with the reduced volume of rare-earth PM material used in the inner rotor.

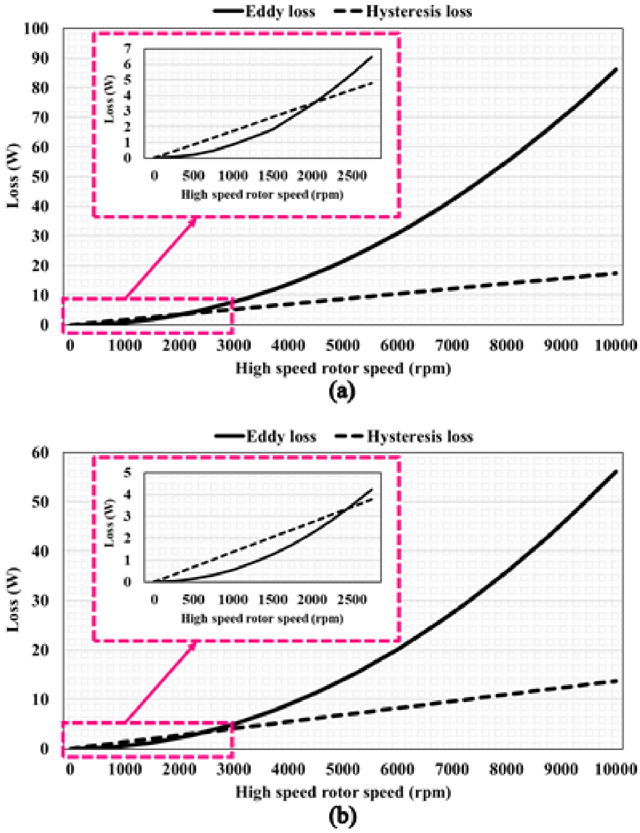

Fig.17. Eddy current losses curve and hysteresis curve in ferromagnetic components. (a) benchmark structure, (b) advanced structure.

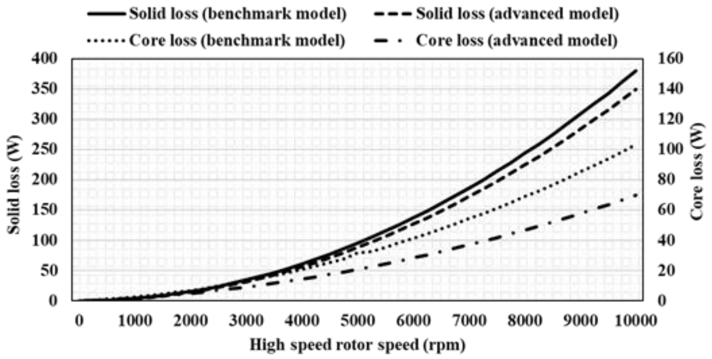

Fig.18. Variation curve of loss and speed

4-6- Mechanical Stress Analysis

The mechanical integrity of the inner rotor must be verified under high-speed operating conditions. Therefore, a structural analysis of the high-speed rotor was performed using ANSYS Workbench 2021-R1. Fig. 19 illustrates the maximum Von Mises stress distribution at different rotational speeds for the proposed CMG structure. The rotor is fabricated from M400-50A non-oriented electrical steel. A yield strength of approximately 350 MPa is adopted for the mechanical analysis based on the material data cited in [58]. This value is not experimentally determined in the present study; rather, it is used as the stress criterion for evaluating the allowable rotational speed of the rotor. Accordingly, the mechanical assessment is based on comparing the maximum Von Mises stress with the adopted yield-strength limit under the mechanical-analysis assumptions considered in this study.

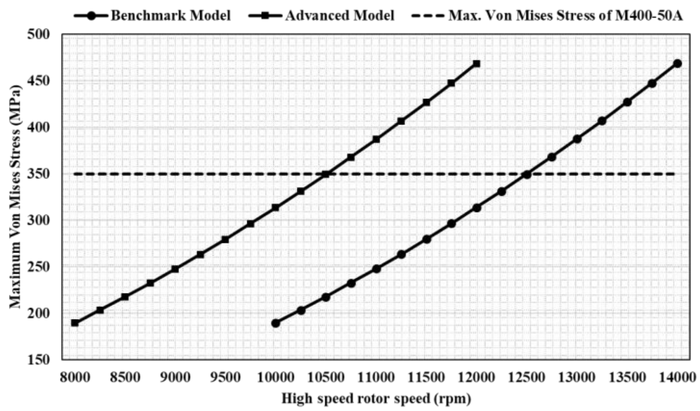

Fig. 19. Maximum Von Mises stress of inner rotor according to the speed of high-speed rotor.

Fig. 19 indicates that the mechanical strength of the proposed advanced rotor decreases with increasing rotational speed. The advanced structure reaches its mechanical limit at approximately 10,500 rpm, whereas the benchmark structure maintains structural integrity up to 12,500 rpm. These results indicate that the benchmark topology provides a larger mechanical safety margin under ultra-high-speed operating conditions. Nevertheless, the proposed advanced structure remains mechanically stable and suitable for operation up to 10,500 rpm, which satisfies the intended operating range of the designed CMG. Fig. 20 presents the Von Mises stress distribution and total deformation of the benchmark and advanced high-speed rotor structures. The benchmark model is evaluated at 12,500 rpm, while the advanced structure is analyzed at 10,500 rpm to compare their mechanical behaviors under their respective operating limits.

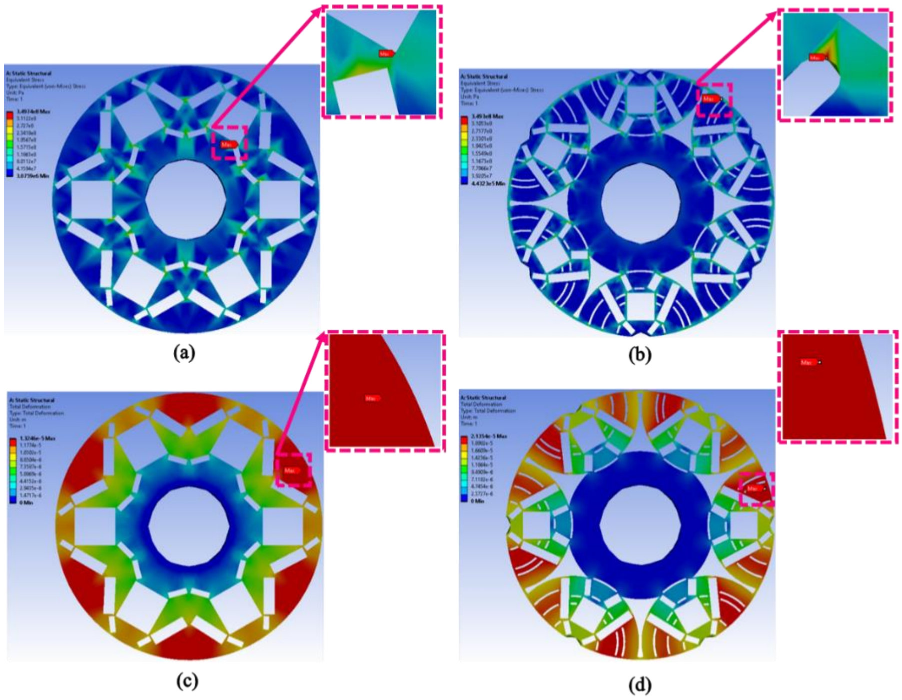

Fig. 20. Mechanical analysis of high-speed rotor. (a) Mises stress distribution of benchmark structure at 12,500 rpm. (b) Mises stress distribution of advanced structure at 10,500 rpm. (c) Total deformation distribution of benchmark structure at 12,500 rpm. (d) Total deformation distribution of advanced structure at 10,500 rpm.

Fig. 20 demonstrates distinct stress distributions for the benchmark and advanced rotor structures. In the benchmark model, the maximum Von Mises stress is concentrated at the interface between the ferrite and rare-earth PMs in the inner rotor layer, identifying this region as the primary mechanical weak point at rotational speeds above 12,500 rpm. In contrast, the advanced structure exhibits maximum stress concentration near the outer edge of the flux barrier region (zone 3). Although the flux-barrier integration improves the electromagnetic performance of the rotor, it also reduces the maximum mechanically sustainable speed to approximately 10,500 rpm. Beyond this operating limit, zone 3 becomes the most critical failure region. Despite the differences in stress distribution, both structures exhibit maximum deformation in the region extending from the middle-layer rare-earth PMs toward the outer surface of the inner rotor.

5. Experimental Validation and Prototype Evaluation

5-1- Prototype Fabrication and Experimental Setup

To validate the finite-element simulations and verify the feasibility of the proposed CMG designs, both the benchmark and advanced structures were fabricated based on the optimized parameters listed in Table 3. The manufactured inner rotors are shown in Fig. 21. Fig. 22 illustrates the experimental setup, which consists of a driving motor, a torque transducer, and a magnetic powder brake equipped with an internal torque sensor. During the static torque measurements, the low-speed rotor was mechanically locked while the high-speed rotor was rotated incrementally. The resulting torque-angle characteristics are presented in Fig. 23.

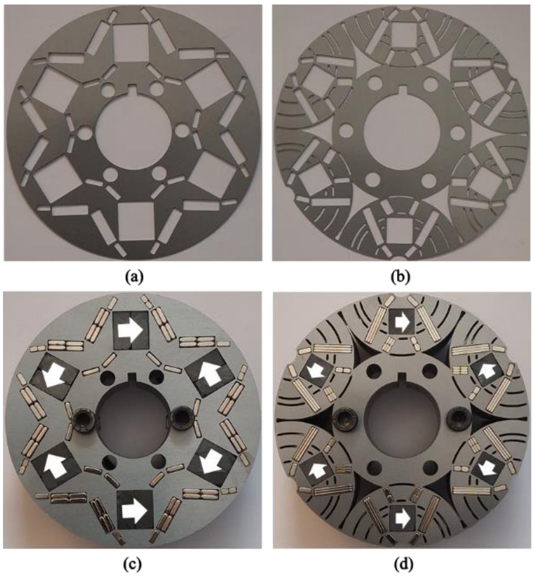

Fig. 21. Inner rotor. (a) Lamination core of benchmark structure. (b) Lamination core of advanced structure. (c) benchmark internal rotor structure with PMs. (d) advanced internal rotor structure with PMs.

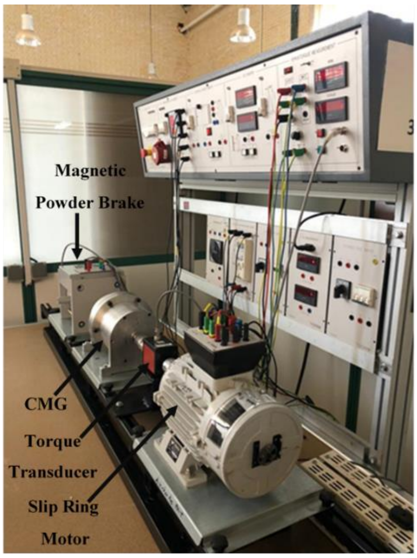

Fig. 22. Magnetic gear test bench

5-2- Static and Dynamic Torque Validation

Fig. 23 demonstrates good agreement between the simulated and experimental torque results for both CMG topologies. For the benchmark structure, the 3-D FEM predicts a maximum inner rotor torque of 8.29 Nm, whereas the experimental measurement yields 7.36 Nm, corresponding to a relative error of 11.2%. Similarly, the advanced structure produces a simulated torque of 8.48 Nm and an experimental torque of 7.61 Nm, resulting in a discrepancy of 10.2%. These differences are mainly attributed to uncertainties in the material properties used in the FEM simulations and manufacturing tolerances associated with the PMs and rotor geometry.

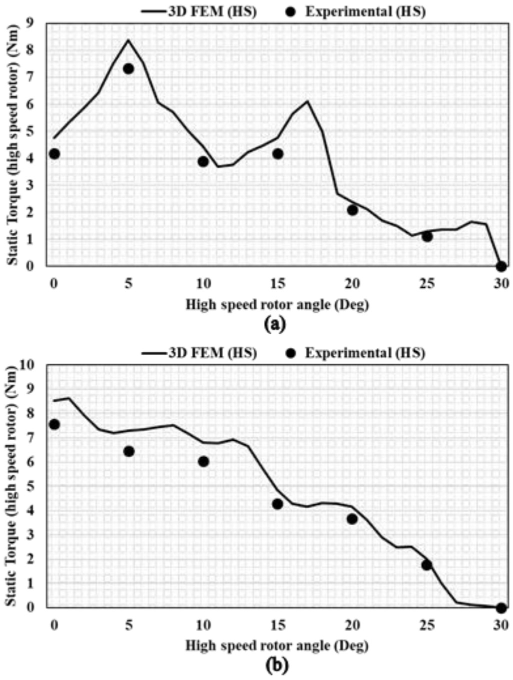

Fig. 23. Static HS torque of experimental and 3-D FEM simulations. (a) benchmark structure (b) advanced structure

Fig. 24 presents the experimentally measured dynamic torque waveforms of the high-speed rotor for the benchmark and advanced CMG structures. Compared with the 2-D and 3-D FEM results, the experimental measurements exhibit higher torque ripple in both topologies.

The experimentally measured cogging torque values are 68.12% and 18.12% for the benchmark and advanced structures, respectively. In comparison, the corresponding 3-D FEM simulations predict cogging torque values of 64.03% and 17.07%. Therefore, the experimental cogging torque exceeds the simulated values by 6.38% for the benchmark structure and 6.15% for the advanced structure.

These discrepancies are mainly attributed to mechanical factors that are not fully considered in the FEM model, including limited stiffness of the bearings and couplings, as well as parasitic vibrations generated by the driving motor.

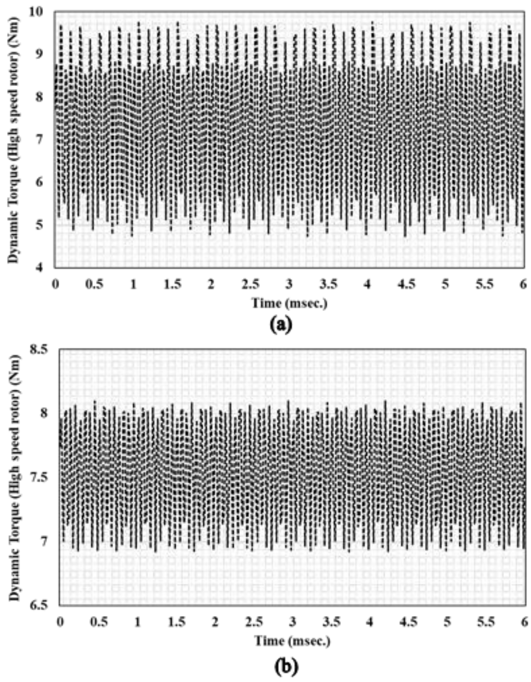

Fig. 24. Experimental dynamic torque of HS rotor (at 1000rpm). (a) benchmark structure (b) advanced structure

As observed in Fig. 24, the average torque and cogging torque of the two configurations are not identical. This difference is attributed primarily to the different PM arrangements and inner-rotor geometries, particularly the flux barriers incorporated into the advanced configuration, which modify the magnetic-flux distribution. Moreover, manufacturing and assembly tolerances, torque-sensor uncertainties, and discrepancies between the fabricated prototype and the idealized FEM model contribute to the differences observed in the experimental torque characteristics.

6. Conclusion

This paper presented a novel hybrid PM CMG featuring a redesigned inner rotor with a series–parallel combination of rare-earth NdFeB and ferrite PMs and fourteen asymmetrically distributed flux barriers. The proposed topology was developed to reduce rare-earth PM utilization while maintaining torque capability and improving torque quality. A multi-objective genetic algorithm coupled with 2-D FEA in ANSYS Maxwell was employed to simultaneously optimize output torque, cogging torque, and PM volume. The optimized results demonstrate that the advanced topology substantially improves PM utilization and torque quality without increasing the overall active volume. In the 3-D FEA, the average high-speed torque increases from 8.29 Nm for the benchmark topology to 8.48 Nm for the Advanced topology, while the cost-equivalent PM volume decreases by 15.7%. The corresponding cogging-torque index is reduced from 64.03% to 17.07%, representing a reduction of approximately 73.3%. Moreover, the TPV increases from 153.23 to 185.96 kNm/m^3, corresponding to a 21.36% improvement. The 2-D FEA yields a similar trend, with a 19.14% improvement in TPV.

The electromagnetic field and loss analyses further verify the effectiveness of the proposed flux-guidance strategy. The flux barriers reduce internal leakage flux, mitigate localized magnetic saturation, and suppress high-order air-gap flux-density harmonics. Consequently, the advanced topology exhibits lower hysteresis and eddy-current losses than the benchmark configuration; at 10,000 rpm, the hysteresis loss decreases from 17.42 to 13.71 W, while the eddy-current loss is reduced by approximately 34.81%.

The mechanical integrity of the high-speed rotor was evaluated using transient structural FEA in ANSYS Workbench 2021-R1, with a 350-MPa yield-strength criterion for M400-50A electrical steel. The maximum allowable rotational speeds were approximately 12,500 rpm for the benchmark and 10,500 rpm for the advanced rotor.

Finally, both configurations were fabricated and experimentally evaluated. The measured static high-speed torque was 7.36 Nm for the benchmark and 7.61 Nm for the Advanced topology, compared with 3-D FEA predictions of 8.29 and 8.48 Nm, respectively, corresponding to errors of 11.2% and 10.2%. Experimental cogging-torque indices of 68.12% and 18.12% for the benchmark and advanced topologies, respectively, were also consistent with the 3-D FEA results.

Overall, the advanced hybrid CMG achieves a favorable trade-off among torque capability, cogging torque, PM-material utilization, and mechanical feasibility. The combination of hybrid PM excitation, optimized magnet placement, and flux barriers enables reduction in rare-earth PM volume and cost-equivalent PM volume (reducing the rare-earth PM volume by 12.5% and the cost-equivalent PM volume by 15.7%) and cogging torque while maintaining a torque level close to the application requirement in the 2-D optimization stage, while the subsequent 3-D analysis quantifies the reduction associated with end effects and axial leakage flux and maintaining sufficient mechanical margin for the target application. Although the advanced topology introduces additional rotor-manufacturing complexity and a lower rotational speed corresponding to the adopted yield-strength criterion, its demonstrated electromagnetic and material-utilization advantages make it a promising candidate for compact magnetic transmission systems, particularly in wind-energy conversion applications.

References

[1] J. -T. Park, T. -W. Lee, D. -K. Hong and J. -H. Chang, "Magnetic–Mechanical Performance Analysis and Experimental Validation of Noncontact Coaxial Magnetic Gear for a Contra-Rotating Propeller in an Electric Outboard," *IEEE Transactions on Magnetics*, vol. 57, no. 2, pp. 1-5, Feb. 2021.
[2] M. Filippini, R. Torchio, P. Alotto, E. Bonisoli, L. Dimauro and M. Repetto, "A New Class of Devices: Magnetic Gear Differentials for Vehicle Drivetrains," *IEEE Transactions on Transportation Electrification*, vol. 9, no. 2, pp. 2382-2397, June 2023.

[3] E. Asahina, K. Mitsuya, K. Nakamura, Y. Tachiya, Y. Suzuki and K. Kuritani, "Demonstration of Ultra-High-Speed Magnetic Gear," *2023 IEEE International Future Energy Electronics Conference (IFEEC)*, Sydney, Australia, 2023.

[4] J. Lee and J. Chang, "Analysis of the Vibration Characteristics of Coaxial Magnetic Gear," *IEEE Transactions on Magnetics*, vol. 53, no. 6, pp. 1-4, June 2017.

[5] S. Xie et al., "A Magnetic-Geared Machine with Improved Magnetic Circuit Symmetry for Hybrid Electric Vehicle Applications," *IEEE Transactions on Transportation Electrification*, vol. 10, no. 1, pp. 2170-2182, March 2024.

[6] K. Iwaki, K. Ito and K. Nakamura, "A Novel Magnetic-Geared Motor Combining Magnetic Gear and SR Motor," *IEEE Transactions on Magnetics*, vol. 59, no. 11, pp. 1-5, Nov. 2023.

[7] K. Li, S. Modaresahmadi, W. B. Williams, J. Z. Bird, J. D. Wright and D. Barnett, "Electromagnetic Analysis and Experimental Testing of a Flux Focusing Wind Turbine Magnetic Gearbox," *IEEE Transactions on Energy Conversion*, vol. 34, no. 3, pp. 1512-1521, Sept. 2019.

[8] H. Baninajar et al., "A Dual-Stack Coaxial Magnetic Gear for a Wave Energy Conversion Generator," *IEEE Transactions on Magnetics*, vol. 58, no. 10, pp. 1-12, Oct. 2022.

[9] B. Praslicka et al., "Design and Analysis of a Novel, Low-Cost, High-Speed Cycloidal Magnetic Gear for Aerospace Servo Actuator Applications," *IEEE/ASME Transactions on Mechatronics*, vol. 28, no. 6, pp. 3352-3363, Dec. 2023.

[10] Armstrong C. G. “Power transmitting device,” US Patent. 687292, 1901.

[11] A. H. Neuland, "Apparatus for transmitting power," USA Patent 1,171,351, 1913.

[12] H. Faus, “Magnet gearing,” U.S. Patent 2 243 555, May 27, 1941.

[13] Y. Wang, M. Filippini, N. Bianchi and P. Alotto, "A Review on Magnetic Gears: Topologies, Computational Models, and Design Aspects," *IEEE Transactions on Industry Applications*, vol. 55, no. 5, pp. 4557-4566, Sept.-Oct. 2019.

[14] M. M. Khaledi, S. A. A. Kashani and M. M. Zaj, "A New Star-Type Rotor Topology in Radial Flux Magnetic Gear," *2024 4th International Conference on Electrical Machines and Drives (ICEMD)*, Tehran, Iran, Islamic Republic of, 2024.

[15] M. M. Khaledi and S. A. A. Kashani, "Mitigation of Cogging Torque in Coaxial Magnetic Gear by Rotors Skew-Shaping," *2025 12th Iranian Conference on Renewable Energies and Distributed Generation (ICREDG)*, Qom, Iran, Islamic Republic of, 2025.

[16] K. Atallah and D. Howe, “A novel high-performance magnetic gear,” IEEE Transactions on Magnetics, vol. 37, no. 4, pp. 2844–2846, 2001.

[17] K. Jenney and S. Pakdelian, "Magnetic Design Aspects of the Trans-Rotary Magnetic Gear Using Quasi-Halbach Arrays," *IEEE Transactions on Industrial Electronics*, vol. 67, no. 11, pp. 9582-9592, Nov. 2020.

[18] M. C. Gardner, B. Praslicka, M. Johnson and H. A. Toliyat, "Optimization of Coaxial Magnetic Gear Design and Magnet Material Grade at Different Temperatures and Gear Ratios," in IEEE Transactions on Energy Conversion, vol. 36, no. 3, pp. 2493-2501, Sept. 2021.

[19] S. V. Sankarraman, A. Daniar and M. Gardner, "Torque Production in Triply-Excited Magnetic Gears," *2023 IEEE International Electric Machines & Drives Conference (IEMDC)*, San Francisco, CA, USA, 2023.

[20] Y. Chen, W. N. Fu and W. Li, "Performance Analysis of a Novel Triple-Permanent-Magnet- Excited Magnetic Gear and Its Design Method," *IEEE Transactions on Magnetics*, vol. 52, no. 7, pp. 1-4, July 2016.

[21] W. N. Fu and L. Li, "Optimal Design of Magnetic Gears with a General Pattern of Permanent Magnet Arrangement," in IEEE Transactions on Applied Superconductivity, vol. 26, no. 7, pp. 1-5, Oct. 2016.

[22] A. Shoaei and Q. Wang, "A Comprehensive Review of Concentric Magnetic Gears," *IEEE Transactions on Transportation Electrification*, vol. 10, no. 3, pp. 5581-5598, Sept. 2024.

[23] S. Khalesidoost, P. Afsari, S. A. Khan and M. C. Gardner, "Comparison of NdFeB, Ferrite, and Hybrid Designs for a Magnetic Continuously Variable Transmission," *2025 IEEE Energy Conversion Conference Congress and Exposition (ECCE)*, Philadelphia, PA, USA, 2025.

[24] M. Chen, K. T. Chau, W. Li, C. Liu and C. Qiu, "Design and Analysis of a New Magnetic Gear With Multiple Gear Ratios," *IEEE Transactions on Applied Superconductivity*, vol. 24, no. 3, pp. 1-4, June 2014.

[25] E. -J. Park, S. -Y. Jung and Y. -J. Kim, "Torque and Loss Characteristics of Magnetic Gear by Bonded PM Magnetization Direction," *IEEE Transactions on Magnetics*, vol. 57, no. 6, pp. 1-4, June 2021.

[26] K. Uppalapati and J. Bird, "A flux focusing ferrite magnetic gear," *6th IET International Conference on Power Electronics, Machines and Drives (PEMD 2012)*, Bristol, 2012.
[27] J. -X. Shen, H. -Y. Li, H. Hao and M. -J. Jin, "A Coaxial Magnetic Gear with Consequent-Pole Rotors," in IEEE Transactions on Energy Conversion, vol. 32, no. 1, pp. 267-275, March 2017.
[28] K. K. Uppalapati, W. B. Bomela, J. Z. Bird, M. D. Calvin and J. D. Wright, "Experimental Evaluation of Low-Speed Flux-Focusing Magnetic Gearboxes," *IEEE Transactions on Industry Applications*, vol. 50, no. 6, pp. 3637-3643, Nov.-Dec. 2014.
[29] M. Chen, K. T. Chau, W. Li and C. Liu, "Cost-Effectiveness Comparison of Coaxial Magnetic Gears with Different Magnet Materials," *IEEE Transactions on Magnetics*, vol. 50, no. 2, pp. 821-824, Feb. 2014.
[30] M. Johnson, M. C. Gardner and H. A. Toliyat, "Design Comparison of NdFeB and Ferrite Radial Flux Surface Permanent Magnet Coaxial Magnetic Gears," *IEEE Transactions on Industry Applications*, vol. 54, no. 2, pp. 1254-1263, March-April 2018.
[31] E. -J. Park, S. -Y. Jung and Y. -J. Kim, "Comparison of Magnetic Gear Characteristics Using Different Permanent Magnet Materials," *IEEE Transactions on Applied Superconductivity*, vol. 30, no. 4, pp. 1-4, June 2020.
[32] B. -C. Bae, S. -Y. Im, S. -H. Lee and M. -S. Lim, "Comparison of Coaxial Magnetic Gears Using Rare Earth and Nonrare Earth Permanent Magnets," *2023 IEEE Transportation Electrification Conference and Expo, Asia-Pacific (ITEC Asia-Pacific)*, Chiang Mai, Thailand, 2023.
[33] A. Al-Qarni, F. Wu and A. El-Refaie, "High-Torque-Density Low-Cost Magnetic Gear Utilizing Hybrid Magnets and Advanced Materials," *2019 IEEE International Electric Machines & Drives Conference (IEMDC)*, San Diego, CA, USA, 2019.
[34] M. M. Khaledi and S. A. A. Kashani, "A New Hybrid Y-Type Rotor Topology for High-Performance Coaxial Magnetic Gear," *2024 4th International Conference on Electrical Machines and Drives (ICEMD)*, Tehran, Iran, Islamic Republic of, 2024.
[35] A. Shoaei, F. Farshbaf-Roomi, Q. Wang and K. Al-Haddad, "Design Optimization of Hybrid Magnet CMGs with Non-Uniform Air-Gap Considering Demagnetization Analysis," *2025 IEEE 34th International Symposium on Industrial Electronics (ISIE)*, Toronto, ON, Canada, 2025.
[36] M. M. Khaledi and S. A. A. Kashani, "Design of an L-Shaped Hybrid PM Array in Coaxial Magnetic Gear," *2025 16th Power Electronics, Drive Systems, and Technologies Conference (PEDSTC)*, Tabriz, Iran, Islamic Republic of, 2025.
[37] X. Zhang, X. Liu, and Z. Chen, "Investigation of Unbalanced Magnetic Force in Magnetic Geared Machine Using Analytical Methods," *IEEE Trans. Magn*, vol. 52, no. 7, pp. 2–5, 2016.
[38] D. Z. Abdelhamid and A. M. Knight, "The Effect of Modulating Ring Design on Magnetic Gear Torque," *IEEE Transactions on Magnetics*, vol. 53, no. 11, pp. 1-4, Nov. 2017.
[39] B. Praslicka, M. C. Gardner, M. Johnson and H. A. Toliyat, "Review and Analysis of Coaxial Magnetic Gear Pole Pair Count Selection Effects," *IEEE Journal of Emerging and Selected Topics in Power Electronics*, vol. 10, no. 2, pp. 1813-1822, April 2022.
[40] B. Dai, K. Nakamura, Y. Suzuki, Y. Tachiya and K. Kuritani, "Cogging Torque Reduction of Integer Gear Ratio Axial-Flux Magnetic Gear for Wind-Power Generation Application by Using Two New Types of Pole Pieces," *IEEE Transactions on Magnetics*, vol. 58, no. 8, pp. 1-5, Aug. 2022.
[41] S. Gerber and R. -J. Wang, "Cogging Torque Definitions for Magnetic Gears and Magnetically Geared Electrical Machines," *IEEE Transactions on Magnetics*, vol. 54, no. 4, pp. 1-9, April 2018
[42] V. MATEEV, M. TODOROVA and I. MARINOVA, "Analysis of Flux Density Harmonic Spectrum of the Coaxial Magnetic Gear," *2019 16th Conference on Electrical Machines, Drives and Power Systems (ELMA)*, Varna, Bulgaria, 2019.
[43] F. Kucuk and S. Mousavi, "Development of a novel Coaxial Magnetic Gear," *2017 15th International Conference on Electrical Machines, Drives and Power Systems (ELMA)*, Sofia, Bulgaria, 2017.
[44] L. Jing, Z. Huang, J. Chen and R. Qu, "An Asymmetric Pole Coaxial Magnetic Gear with Unequal Halbach Arrays and Spoke Structure," *IEEE Transactions on Applied Superconductivity*, vol. 30, no. 4, pp. 1-5, June 2020.
[45] S. Zheng, X. Zhu, L. Xu, Z. Xiang, L. Quan and B. Yu, "Multi-Objective Optimization Design of a Multi-Permanent-Magnet Motor Considering Magnet Characteristic Variation Effects," *IEEE Transactions on Industrial Electronics*, vol. 69, no. 4, pp. 3428-3438, April 2022.
[46] T. Sharifi, A. Jamali-Fard and H. A. Moghaddam, "Multi-Objective Design Optimization of a Flux-Switching Permanent Magnet Motor: A Comparative Study of Metaheuristic Algorithms," *2025 5th International Conference on Electrical Machines and Drives (ICEMD)*, Tehran, Iran.

[47] J. Cheon, S. B. Bae and S. G. Min, "Analytical Modeling and Optimization of PM Synchronous Machines Using Novel R262-TLBO Algorithm," *IEEE Transactions on Magnetics*, vol. 59, no. 12, pp. 1-16, Dec. 2023.
[48] M. -F. Hsieh, A. T. Huynh, V. -V. Do, D. Gerada and C. Gerada, "Design Optimization of Spoke-Type Flux-Intensifying PM Motor With Asymmetric Rotor Configuration for Improved Performance," *IEEE Transactions on Magnetics*, vol. 60, no. 9, pp. 1-5, Sept. 2024.
[49] A. Toffolo and E. Benini, "Genetic Diversity as an Objective in Multi-Objective Evolutionary Algorithms," in Evolutionary Computation, vol. 11, no. 2, pp. 151-167, June 2003.
[50] L. dos Santos Coelho and P. Alotto, "Multiobjective Electromagnetic Optimization Based on a Nondominated Sorting Genetic Approach With a Chaotic Crossover Operator," *IEEE Transactions on Magnetics*, vol. 44, no. 6, pp. 1078-1081, June 2008.
[51] B. Raj, I. Ahmedy, M. Y. I. Idris and R. M. Noor, "A Hybrid Sperm Swarm Optimization and Genetic Algorithm for Unimodal and Multimodal Optimization Problems," *IEEE Access*, vol. 10, pp. 109580-109596, 2022.
[52] X. Zhu, W. Wu, L. Quan, Z. Xiang and W. Gu, "Design and Multi-Objective Stratified Optimization of a Less-Rare-Earth Hybrid Permanent Magnets Motor With High Torque Density and Low Cost," *IEEE Transactions on Energy Conversion*, vol. 34, no. 3, pp. 1178-1189, Sept. 2019.
[53] S. A. M. Ali, M. N. Hamidon, and M. F. Omar, “Simplified Design of Magnetic Gear by Considering the Maximum Transmission Torque Line,” *Applied Sciences*, vol. 10, no. 23, Art. no. 8581, 2020.
[54] S. A. Afsari Kashani, "Design and Optimization of Coaxial Reluctance Magnetic Gear With Different Rotor Topologies," *IEEE Transactions on Industrial Electronics*, vol. 69, no. 1, pp. 101-109, Jan. 2022.
[55] E. Asahina, Y. Tachiya and K. Nakamura, "Eddy Current Loss Reduction in Flux-Modulated-Type Magnetic Gears by Unequal Division of Magnets," *IEEE Transactions on Magnetics*, vol. 61, no. 9, pp. 1-5, Sept. 2025.
[56] Y. Tian, G. Liu, W. Zhao and J. Ji, "Design and Analysis of Coaxial Magnetic Gears Considering Rotor Losses," *IEEE Transactions on Magnetics*, vol. 51, no. 11, pp. 1-4, Nov. 2015.
[57] V. Mateev, M. Todorova and I. Marinova, "Eddy Current Losses of Coaxial Magnetic Gears," *2018 XIII International Conference on Electrical Machines (ICEM)*, Alexandroupoli, Greece, 2018.
[58] H. Tiismus, A. Kallaste, T. Vaimann, L. Lind, I. Virro, A. Rassõlkin, and T. Dedova, “Laser additively manufactured magnetic core design and process for electrical machine applications,” *Energies*, vol. 15, no. 10, Art. no. 3665, May 2022.